

國立交通大學

物理研究所

博士論文



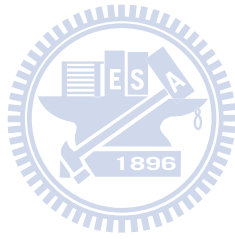
在單根金屬氧化物奈米線中的電子傳輸過程

Electron transport processes in individual  
metal oxide nanowires

研究生：邱劭斌

指導教授：林志忠 教授

中華民國九十九年七月



在單根金屬氧化物奈米線中的電子傳輸過程

Electron transport processes in individual  
metal oxide nanowires

研究生：邱劭斌

Student：Shao-Pin Chiu

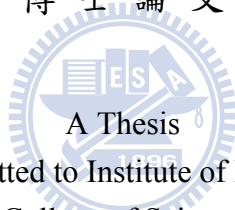
指導教授：林志忠

Advisor：Juhn-Jong Lin

國立交通大學

物理研究所

博士論文



Submitted to Institute of Physics  
College of Science

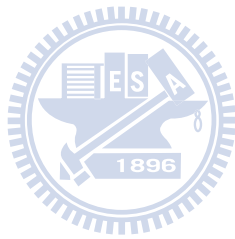
National Chiao Tung University  
in Partial Fulfillment of the Requirements  
for the Degree of  
Doctor  
In

Physics

July 2010

Hsinchu, Taiwan, Republic of China

中華民國九十九年七月



# 在單根金屬氧化物奈米線中的電子傳輸過程

學生：邱劭斌

指導教授：林志忠 教授

國立交通大學物理研究所博士班

## 摘 要

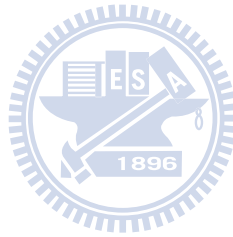
在本篇論文中，我們研究了單根的氧化銻錫、氧化鋅、以及摻雜銻或鉛的氧化鋅奈米線的本徵導電性質。這些單晶的奈米線可以經由熱蒸鍍或雷射輔助的化學氣相沈積的方式合成。鈦/金或鉻/金微電極可利用電子束微影技術製作於單根奈米線上。利用四點量測的方式，300 K 到 0.25 K 之間的電阻，以及 70 K 到 0.25 K 之間的磁電阻，可以被有系統的量測與分析。

氧化銻錫奈米線的值經約為 110 ~ 220 奈米。從 300 K 到 1.5 K 的電阻率隨溫度的變化可以用 Bloch-Grüneisen 定律加上一個低溫區的修正項來描述。這個低溫修正項反映著動態的點缺陷的存在，以及電子被這些缺陷所散射導致了電阻率隨溫度下降而有較劇烈的上升變化。

氧化鋅奈米線的值經約為 90 ~ 200 奈米。雖然我們沒有特意對它們做摻雜，但成長時所自然生成的缺陷卻可以提供載子，而導致不同的電阻率。電阻率較大的樣品我們稱之為半導體性的。它們的電阻率和溫度的關係可以用三個  $\rho_i^{-1} \exp(-E_i/k_B T)$  項的相加來描述 ( $i=1, 2, 3$ )。其中  $E_i$  是特徵能量，且  $E_1 > E_2 > E_3$ 。電子從費米面被熱激發到導帶，以及一個分裂的雜質能帶 (upper  $D^-$  band) 上的過程分別對應到  $E_1$  以及  $E_2$  項。而費米面附近的最近鄰跳躍導電則對應到  $E_3$  項。電阻率最小的一個樣品則已經呈現金屬的某些特性，並且其導電是和表面相關的。

摻雜銻以及鉛的氧化鋅奈米線 (直徑約 70 ~ 90 nm) 已經表現出簡併費米氣體 (degenerate Fermi gas) 的特性。我們發現 70 K 到 0.25 K 之間的中間溫區的磁電阻必須要用二維的弱局域效應才能合理的分析。而在這個溫區

的兩端的低溫區以及高溫區，則分別要以一維和三維的弱局域效應來描述。在比較中間溫區的垂直磁場以及平行磁場的磁電阻後，我們可以定量分析出一個特徵厚度  $t$ ，它對應到奈米線中的某種二維的結構。因此我們假設奈米線有類似中心核-外殼(core-shell)的結構。 $t$  就對應到殼的厚度。因此，當相位同調長度  $L_\phi$  和厚度  $t$  接近時，就會發生弱局域效應的維度的轉變。類似的情形也發生在另一個量子干涉效應，電子-電子交互作用(EEI)上。當 EEI 的特徵長度，熱擴散長度  $L_T$ ，和厚度  $t$  接近時，也會導致 EEI 的維度改變。由磁電阻的分析可以得到同調相位破壞率  $\tau_\phi^{-1}$  和溫度的關係 ( $\tau_\phi^{-1}(T) \sim T^p, 1 < p < 1.5$ )。這樣的  $p$  值可能是來自於大能量交換的電子-電子散射，或是聲子維度受限時的電子-聲子散射。另外，我們發現其中一個摻雜鉛的氧化鋅奈米線的 I-V 曲線在低偏壓區有明顯的非線性存在。我們把它歸因於某種穿越中心核和殼的邊界的導電過程。



# Electron transport processes in individual metal oxide nanowires

Author:

Shao-Pin Chiu

Thesis advisor:

Dr. Juhn-Jong Lin

Institute of Physics  
National Chiao Tung University

## Abstract

The intrinsic electrical transport properties of individual nanowires (NWs), including ITO, ZnO, and (In,Pb)-doped ZnO NWs, are studied in this thesis. These single-crystalline NWs were synthesized by either the thermal evaporation method or the laser-assisted chemical vapor deposition (CVD) method. Four-probe Ti/Au or Cr/Au electrodes were fabricated by the electron-beam lithography technique. The resistances between 300 and 0.25 K and the magnetoresistances (MRs) between 70 and 0.25 K of these NWs have been systematically studied.

The temperature dependent resistivities,  $\rho(T)$ , of four ITO NWs with diameters of 110 to 220 nm and lengths of a few  $\mu\text{m}$  long have been measured. The results indicate that the as-grown ITO NWs are metallic, but disordered. The overall temperature behavior between 300 and 1.5 K can be described by the Bloch–Grüneisen law plus a low-temperature correction due to the scattering of electrons off dynamic point defects. This observation suggests the existence of numerous dynamic point defects in as-grown ITO NWs.

For the nominally undoped ZnO NWs with diameters of 90 to 200 nm, the temperature behavior of  $\rho(T)$  between 300 and 5 K reveals that the electrical-transport mechanisms are due to a combination of the thermal activation conduction and the nearest-neighbor hopping conduction processes. Three distinct activation and hopping contributions with discrete

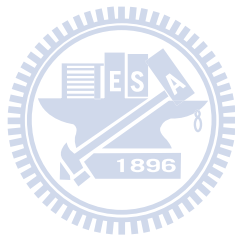
characteristic activation energies are observed. Above about 100 K, the charge transport mechanism is dominated by the thermal activation of electrons from the Fermi level,  $\mu$ , to the conduction band. Between approximately 20 and 100 K, the charge transport mechanism is due to the activation of electrons from  $\mu$  to the upper impurity ( $D^-$ ) band. Between approximately 5 and 20 K, the charge transport mechanism arises from the nearest-neighbor hopping conduction within the lower impurity ( $D$ ) band. Such unique electrical conduction behaviors can be explained in terms of the intricate material properties (in particular, the presence of moderately high concentrations of n-type defects accompanied with a slight self-compensation) in natively doped ZnO NWs. In one heavily doped NW, a surface-related conduction process manifesting the two-dimensional attributes of quantum-interference transport phenomena is observed. The carrier concentrations in our NWs have been estimated, and they were found to lie close to the critical concentration for the Mott metal–insulator transition.

The indium- and lead-doped ZnO NWs with diameters of 70 to 90 nm showed behavior of degenerate Fermi gas of their resistivities,  $\rho(T)$ . We have measured the MRs of several doped ZnO NWs between 0.25 and 70 K in magnetic fields with directions both perpendicular and parallel to the wire axes. Our quantitative analysis showed that we have to utilize the weak-localization (WL) effects of different dimensionalities to explain the MRs in different ranges of temperature. Otherwise, the MRs can not be satisfactorily described. A characteristic length, named the effective wire width,  $a$ , extracted from one-dimensional (1D) WL effect has been introduced. From the perpendicular and parallel MRs, another characteristic length, named the effective film thicknesses,  $t$ , was extracted under the framework of the two-dimensional (2D) WL effect. Hence, a core-shell-like structure inside individual nanowires is suggested. Within this model, as the electron phase-coherent length,  $L_\phi$ , decreases with increasing temperature, a 1D-to-2D dimensional crossover of the WL effect occurs around the characteristic temperature where  $L_\phi \sim a$ , and also a 2D-to-3D dimensional crossover occurs around another characteristic temperature where  $L_\phi \sim t$ . The exponent of temperature,  $p$ , of the electron dephasing rate,  $\tau_\phi^{-1}$ , has been determined. The result suggests



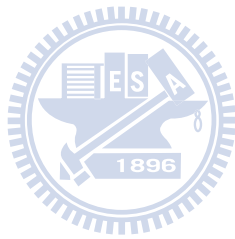
that the dephasing mechanisms could be due to the electron-electron (e-e) scattering with large energy transfer or the electron-phonon (e-ph) scattering with reduced phonon dimensionality. In addition, the core-shell-like structure has been verified from the temperature behaviors of low-temperature resistivities in a moderately high magnetic field, which demonstrated the dominating electron-electron interaction (EEI) effect. A dimensional crossover of EEI was also observed under the condition that the thermal diffusion length,  $L_T$ , became close to the shell thickness  $t$ . In a lead-doped ZnO NW, the nonlinearity of the I-V curves around zero-bias is attributed to the 2D property of relatively small shell thickness and the electron motion across the core-shell interface.





感謝所有幫助過我的人





# Contents

<b>Abstract</b> .....	v
<b>List of Tables</b> .....	xv
<b>List of Figures</b> .....	xvii
<b>1 Introduction</b> .....	1
<b>2 Sample fabrication and measurement setup</b> .....	5
2.1 Growth of nanowires (NWs).....	5
2.2 Fabrication of single NW devices .....	5
2.3 Methods of electrical measurements .....	7
<b>3 Electrical transport in ITO nanowires</b> .....	13
3.1 Introduction .....	13
3.2 Experimental method .....	14
3.2 Results and discussion .....	19
3.4 Summary .....	29
<b>4 Electrical transport in natively doped ZnO nanowires</b> .....	31
4.1 Introduction .....	31
4.2 Experimental method .....	32
4.3 Results and discussion .....	36
4.3.1 Semiconducting ZnO nanowires .....	36
4.3.2 'Metallic-like' ZnO nanowire and surface-related conduction .....	44
4.3.3 Estimate of carrier concentrations and surface-related conduction .....	47
4.4 Summary .....	48
<b>5 Electrical transport in doped ZnO nanowires</b> .....	51
5.1 Introduction .....	51
5.2 Theoretical background.....	51
5.2.1 Weak localization effect and the related magnetoresistance .....	51
5.2.2 dephasing mechanisms .....	54

5.2.3 Electron-electron interaction .....	56
5.3 Indium-doped ZnO (In:ZnO) nanowires .....	57
5.3.1 Sample information .....	57
5.3.2 Magnetoresistance and weak localization effect .....	61
5.3.3 Dephasing rate .....	76
5.3.4 Inner structure of nanowires .....	79
5.3.5 Dimensional crossover of electron-electron interaction .....	84
5.4 Lead-doped ZnO (Pb:ZnO) nanowires .....	89
5.4.1 Sample information .....	89
5.4.2 Magnetoresistance and dephasing rate .....	89
5.4.3 Electron-electron interaction and the nonlinearity of I-V curves .....	96
5.5 Summary .....	100
<b>6 Conclusion</b> .....	<b>103</b>
<b>References</b> .....	<b>105</b>



## List of Tables

**Table 3.1:** Relevant parameters for four-probe individual ITO NW devices.  $T_s$  is the Si substrate temperature during the NW growth process. The character in parentheses following the temperature indicates the substrate name, A or B. Sn/In is the weight ratio of tin to indium.  $d$  is the NW diameter.  $\rho_{\min}$  is the lowest measured resistivity of each sample.  $T_{\min}$  is the temperature where  $\rho_{\min}$  occurred. .... 16

**Table 3.2:** Least-squares fitted ( $\rho_0$ ,  $\theta D$  and  $\beta$ ) and evaluated ( $l$  and  $kFl$ ) values of relevant parameters for individual ITO NWs. .... 23

**Table 4.1:** Values of relevant parameters for four natively doped, single-crystalline ZnO NWs and a bulk single crystal. The three Z-L011, Z-f-R and Z-k1 NWs are referred to as ‘semiconducting’ NWs, while the Z-d-L NW is referred to as a ‘metallic-like’ NW. Owing to uncertainties in the NW dimensions, the absolute values of  $\rho$  (300 K) are accurate to  $\approx 10\%$ . .... 35

**Table 5.1(a):** Parameters for the doped-ZnO nanowire devices.  $dia.$  is the nanowire diameter,  $L$  is the nanowire length between the two voltage electrodes in the four-probe configuration,  $R$  (300 K) is the resistance at 300 K,  $\rho$  (300 K) and  $\rho$  (10 K) are the resistivities at 300 K and 10 K, respectively,  $n$  is the carrier concentration estimated from  $\rho$  (10 K),  $l$  is the electron mean free path, and  $D$  is the electron diffusion constant. The values of  $l$  and  $D$  are calculated from  $\rho$  (10 K) and  $n$ . .... 59

**Table 5.1(b):** Parameters for the doped-ZnO nanowire devices.  $l(\tau)$  is the electron mean free path (time),  $k_F$  is the Fermi wavenumber,  $v_F$  is the Fermi velocity,  $E_F$  is the Fermi energy,  $\lambda_F$  is the Fermi wavelength,  $k_F l$  is the value by multiplying  $k_F$  and  $l$ , and  $L_T$  is the thermal diffusion length which defined as  $L_T = \sqrt{D\hbar/k_B T}$ . .... 59

**Table 5.2:** Parameters from the curve fitting of MRS.  $L_\phi$  is the phase coherent length,  $L_{so}$  is the spin-orbit scattering length,  $a$  is the effective wire width for 1D WL effect in perpendicular magnetic field,  $w$  is the effective film width for 2D WL effect in perpendicular magnetic field, and  $t$  is the effective film thickness for 2D WL effect in parallel magnetic field. .... 70

**Table 5.3.** Parameters from the curve fitting.  $\tau_0$ ,  $A$ , and  $p$  are the parameters related to the dephasing rate  $\tau_\phi^{-1}$  in Eq. (5.8a).  $\tilde{F}$  is the coupling constant of Hartree processes defined in Eq. (5.7). ..... 78





# List of Figures

**Figure 2.1:** A schematic flow chart of fabricating the single NW devices. .... 6

**Figure 2.2:** Two samples are fixed on the sample holder of  $^3\text{He}$  cryostat. There are two areas for different magnetic field orientations. The left-up inset is a SEM image of a single ZnO NW device. The scale bar is  $5\ \mu\text{m}$ . The right-down inset is the whole view of a sample on which several copper wires are already connected. .... 8

**Figure 2.3:** The equivalent circuits for two- and four- probe measurement. The  $R_i$ ,  $i=1, 2, 3$ , are the NW resistances in different segments. The  $R_{ci}$ ,  $i=1, 2, 3, 4$ , are the contact resistances within different interfaces between NW and metal electrodes. .... 9

**Figure 2.4:** The measurement process is controlled by a LabVIEW program which is functionalized to control the temperatures and measure the resistances and  $I$ - $V$  curves at stable temperatures. .... 11

**Figure 3.1:** (a) A low magnification TEM image for a single ITO NW. (b) A high-resolution TEM image for the same ITO NW. The inset shows the corresponding selected-area electron diffraction pattern. (c) EDS spectrum for the ITO NWs grown on substrate A. The Cu peaks are due to the TEM Cu grids. .... 15

**Figure 3.2:** Current–voltage curves for the individual ITO-c-R NW at 297 and 4.2 K, as indicated. Notice that the  $I$ - $V$  curves are linear. The inset shows an SEM image for this four-probe ITO NW device fabricated with electron-beam lithography. The scale bar is  $5\ \mu\text{m}$ . .... 17

**Figure 3.3:** Measured two-probe,  $R_{2p}$ , and four-probe,  $R_{4p}$ , resistances as a function of

temperature for the individual ITO-c-R NW devices, as indicated. The two-probe data were measured with the two inner electrodes as depicted in the inset to [figure 3.2](#). The dashed line indicates the total contact resistance plus the lithographic electrode resistance, as given by  $R_c(T) = R_{2p}(T) - R_{4p}(T)$ . ..... 20

**Figure 3.4:** Normalized resistivities,  $\rho(T)/\rho(300\text{ K})$ , as a function of temperature for four individual ITO NWs, as indicated. The symbols are the experimental data and the solid curves are the theoretical predictions of [equation \(3.1\)](#). The inset shows the measured resistivity as described by the sum of the Bloch–Grüneisen law (solid curve) and a disorder-induced correction to  $\rho_0$  (dashed curve) for the ITO-c-R NW ..... 21

**Figure 3.5:** Normalized resistivities,  $\rho(T)/\rho_{\min}$ , as a function of temperature for four individual ITO NWs, as indicated. Notice that the resistivity rises scale approximately with  $\sqrt{T}$ . For the ITO-j1 NW, there is a tendency to saturation below about 10 K, while for the ITO-g NW, there is an abrupt resistivity drop at 5 K. ..... 25

**Figure 3.6:** Resistance as a function of temperature for the ITO-g NW in zero magnetic field and in two magnetic fields of 0.79 and 1.5 T, as indicated. The magnetic fields were applied perpendicular to the direction of the current flow. .... 27

**Figure 4.1:** (a) An image of scanning electron microscope (SEM) of the as-grown NWs. The inset shows that the wire cross section is circular and with diameter around 100 nm. (b) A high-resolution transmission electron microscopy (TEM) image. The inset shows the corresponding selected-area electron diffraction pattern. (c) The schematic view of wurtzite crystal structure inside ZnO NWs. .... 33

**Figure 4.2:** Variation of resistivity with temperature for four ZnO NWs and a bulk ZnO single crystal. The inset shows the current–voltage curves for the Z-k1 NW at 300, 30, 20, 10

and 4.5 K. Also shown is a SEM image for a four-probeNW device fabricated with electron-beam lithography. The scale bar is 5  $\mu\text{m}$ . Notice that the resistivities of the natively doped NWs are several orders of magnitude lower than that of the bulk. .... 34

**Figure 4.3:** (a) Variation of resistivity with reciprocal temperature for three semiconducting ZnO NWs between 300 and 4 K. The solid curves are least-squares fits to equation (4.1). The straight dashed lines indicate the three contributions given by equation (4.1) for each NW. (b) Variation of resistivity with reciprocal temperature for the same three semiconducting ZnO NWs between 300 and 0.4 K. Notice that the resistivity essentially approaches a constant below 2–4 K in each NW. The solid curves are guides to the eye. In both (a) and (b), for clarity, the resistivity of the Z-k1 NW has been vertically shifted up by multiplying a factor of 10, while the resistivity of the Z-L011 NW has been vertically shifted down by multiplying a factor of 0.1. .... 37

**Figure 4.4:** Schematic electronic density of states (DOS) diagram depicting the conduction band ( $E_1$ -conduction) and the upper D band ( $E_2$ -conduction) processes. The impurity band splits into two bands: the lower D band and the upper  $D^-$  band. If disorder is strong enough, the band tails will smear and overlap, leading to localized regimes with finite DOS (as hatched with dotted lines). In the case of a weak compensation, the Fermi level  $\mu$  lies near the top edge of the lower D band. The presence of a small number of unoccupied donor levels which lie just above  $\mu$  is not explicitly indicated. (See, for example, references [24] and [26]. .... 39

**Figure 4.5:** Normalized resistance,  $\Delta R(T)/R(20\text{ K}) = [R(T) - R(20\text{ K})]/R(20\text{ K})$ , as a function of temperature for the metallic-like Z-d-L NW, where  $R(20\text{ K}) = 98.6\text{ k}\Omega$ . The straight solid line is a least-squares fit to the two-dimensional weak-localization and electron–electron interaction effects. The inset shows the normalized sheet magnetoresistance,  $\Delta R_{\square}(B)/R_{\square}^2(0) = [R_{\square}(B) - R_{\square}(0)]/R_{\square}^2(0)$ , for the same NW at 4.2 K. The solid curve is a

least-squares fit to the two-dimensional weak-localization magnetoresistance theory (see text).  
 ..... 43

**Figure 4.6:** Magnetoresistivity as a function of the square of magnetic field for the Z-k1 NW at 0.255 K (triangles), and the Z-L011 NW at 4.24 K (circles). The straight solid lines are least-squares fits to the data. .... 46

**Figure 5.1:** (a) A SEM image of the as-grown In:ZnO nanowires on the silicon substrate. (b) A high-resolution TEM image for a single nanowire. The inset shows the corresponding selected-area electron diffraction pattern. (c) EDX spectrum of In:ZnO nanowires. The indium to zinc atomic ratio is around 3%. .... 58

**Figure 5.2:** (a) Compare the temperature behaviors of the resistivity of undoped-ZnO nanowires and doped-ZnO nanowires. The upper three curves belong to the undoped-ZnO nanowires. The lower three curves belong to doped-ZnO nanowires. (b) Zoom in to show the three curves of doped-ZnO nanowires in detail. IZOa and IZO b are the samples of In-doped ZnO nanowires. PZO e is the sample of Pb-doped ZnO nanowires. .... 60

**Figure 5.3:** For sample IZOa. (a) Magnetoresistances as a function of perpendicular magnetic field at different temperatures. The inset shows an SEM image of IZOa nanowire device. We perform four-probe measurement through the four electrodes marked by  $I^+$ ,  $V^+$ ,  $V^-$ ,  $I^-$ . The scale bar is 1  $\mu\text{m}$ . (b) Magnetoresistances as a function of *parallel* magnetic field at different temperatures. .... 62

**Figure 5.4:** For sample IZO b. (a) Magnetoresistances as a function of perpendicular magnetic field at different temperatures. The inset shows an SEM image of IZO b nanowire device. The scale bar is 1  $\mu\text{m}$ . (b) Magnetoresistances as a function of *parallel* magnetic field at different temperatures. .... 63

**Figure 5.5:** For sample IZOa. The symbols are the MR data in the perpendicular magnetic field. (a) The solid curves are the theoretical curves predicted by the 1D WL effect (Eq. (5.1)). (b) The solid curves are the theoretical curves predicted by the 3D WL effect (Eq. (5.4)). For clearer view, the result of 8 K is moved to the inset. .... 65

**Figure 5.6:** For sample IZOa. Figures (a), (b), (c), (d), (e), and (f) correspond to temperatures 0.26 K, 0.26 K, 0.26 K, 10 K, 40 K, and 70 K, respectively. Square symbols are the MRs of perpendicular magnetic field. Circle symbols are the MRs of parallel magnetic field. Solid and dashed curves are the theoretical curves predicted by the WL effects in the perpendicular and parallel magnetic fields, respectively. .... 66

**Figure 5.7:** For sample IZOa. (a) The symbols are the MR data of 0.26 K. Solid curve is the theoretical curve by Eq. (5.1). Dashed curve is the theoretical curve by Eq. (5.2). Inset is the plot under  $B^2$  x-axis. (b) The symbols are the MR data of 40 K. Solid curve is the theoretical curve by Eq. (5.2). Dashed curve is the theoretical curve by Eq. (5.4). .... 67

**Figure 5.8:** For sample IZOa, the symbols are the MR data of perpendicular magnetic field. Solid curves are the theoretical curves predicted by the 2D WL effect (Eq. (5.2)). .... 68

**Figure 5.9:** For sample IZOa. (a) The extracted phase coherent lengths,  $L_\phi$ 's, as a function of temperature. Dashed and dotted lines mark the effective wire width,  $a$ , and effective film thickness,  $t$ . (b) Dephasing rates transferred from selected  $L_\phi$ 's as a function of temperature. The solid curve is theoretical curve by Eq. (5.8a). .... 69

**Figure 5.10:** For sample IZOa. The symbols are the MR data in the perpendicular magnetic field. (a) The solid curves are the theoretical curves predicted by the 1D WL effect (Eq. (5.1)). (b) The solid curves are the theoretical curves predicted by the 3D WL effect (Eq. (5.4)). (c)

Solid curves are the theoretical curves predicted by the 2D WL effect (Eq. (5.2)). ..... 73

**Figure 5.11:** For sample IZO<sub>b</sub>. (a) The symbols are the MR data of 7 K. Solid curve is the theoretical curve by Eq. (5.1). Dashed curve is the theoretical curve by Eq. (5.2). (b) The symbols are the MR data of 50 K. Solid curve is the theoretical curve by Eq. (5.2). Dashed curve is the theoretical curve by Eq. (5.4). ..... 74

**Figure 5.12:** For sample IZO<sub>b</sub>. (a) The extracted phase coherent lengths,  $L_\phi$ 's, as a function of temperature. Dashed and dotted lines mark the effective wire width,  $a$ , and effective film thickness,  $t$ . (b) Dephasing rates transferred from selected  $L_\phi$ 's as a function of temperature. The solid curve is theoretical curve by Eq. (5.8a). ..... 75

**Figure 5.13:** For sample IZO<sub>a</sub>. (a) The symbols are the MR data in the parallel magnetic field. The solid curves are the theoretical curves predicted by the 2D WL effect (Eq. (5.3)). (b) The extracted effective film thicknesses as a function of temperature. The average value is 17.3 nm. The inset is a scheme of core-shell-like structure inside the nanowires. ..... 80

**Figure 5.14:** For sample IZO<sub>b</sub>. Figures (a), (b), (c), and (d) correspond to temperatures 0.26 K, 3.0 K, 20 K, and 50 K, respectively. Square symbols are the MRs of perpendicular magnetic field. Circle symbols are the MRs of parallel magnetic field. Solid and dashed curves are the theoretical curves predicted by the WL effects in the parallel and perpendicular magnetic fields, respectively. ..... 81

**Figure 5.15:** For sample IZO<sub>b</sub>. (a) The symbols are the MR data in the parallel magnetic field. The solid curves are the theoretical curves predicted by the 2D WL effect (Eq. (5.3)). (b) The extracted effective film thicknesses as a function of temperature. The average value is 15.5 nm. .... 82

**Figure 5.16:** For sample IZOa. (a) The resistivities as functions of temperature in the 0-Tesla and 4-Tesla magnetic fields are plotted with  $T^{1/2}$  x-axis. (b) The modified conductivities based on the Eq. (5.7) are plotted with  $T^{1/2}$  x-axis. .... 85

**Figure 5.17:** For sample IZOa. (a) The resistivities as functions of temperature in the 0-Tesla and 4-Tesla magnetic fields. (b) The resistivities in the 4-Tesla magnetic field are plotted with  $T^{1/2}$  x-axis. Solid curve is the theoretical curve predicted by Eq. (5.7). (c) The resistivities in the 4-Tesla magnetic field are plotted with logarithmic x-axis. Solid curve is the theoretical curve predicted by Eq. (5.7). .... 86

**Figure 5.18:** The symbols are the theoretical predicted values of thermal diffusion length,  $L_T$ , for sample IZOa and IZOa. The dashed and dotted lines correspond to effective film thicknesses of IZOa and IZOa. Data of wider temperature range is shown in the inset. .... 87

**Figure 5.19:** For sample PZOe, (a) A SEM image of the as-grown Pb:ZnO nanowires on the silicon substrate. (b) A high-resolution TEM image for a single nanowire. (c) EDX spectrum of Pb:ZnO nanowires. The lead to zinc atomic ratio is around 0.62%. .... 90

**Figure 5.20:** For sample PZOe, magnetoresistances as a function of perpendicular magnetic field at different temperatures. The inset shows an SEM image of the nanowire device. We perform four-probe measurement through the four electrodes marked by  $I^+$ ,  $V^+$ ,  $V^-$ ,  $I^-$ . The scale bar is 1  $\mu\text{m}$ . .... 91

**Figure 5.21:** For sample PZOe, the time-dependent resistances at different temperatures. 92

**Figure 5.22:** For sample PZOe. The symbols are the MR data in the perpendicular magnetic field. (a) The solid curves are the theoretical curves predicted by the 1D WL effect (Eq. (5.1)). (b) The solid curves are the theoretical curves predicted by the 3D WL effect (Eq. (5.4)). (c)

Solid curves are the theoretical curves predicted by the 2D WL effect (Eq. (5.2)) The inset shows the data of 20 K and the theoretical curves predicted by 1D and 2D WL effects. .... 94

**Figure 5.23:** For sample PZOe. (a) The extracted phase coherent lengths,  $L_\phi$ 's, as a function of temperature. Dashed line marks the effective wire width,  $a$ . (b) Dephasing rates transferred from selected  $L_\phi$ 's as a function of temperature. The solid curve is theoretical curve by Eq. (5.8a). ..... 95

**Figure 5.24:** For sample PZOe, The symbols are the resistivities as functions of temperature in the 0-Tesla and 4-Tesla magnetic fields. Solid curve is the theoretical curve predicted by Eq. (5.7) ..... 96

**Figure 5.25:** For sample PZOe. (a) The I-V curves at different temperatures. Inset is the zoom-in of high-bias region. (b) The  $G(V)$  differentiated from I-V curves at different temperatures. .... 98

**Figure 5.26:** For sample PZOe. (a) The  $G(V)$  differentiated from I-V curves at 1.35 K. Dashed curves is described by  $G(V)=a+b*\ln V$ . (b) The same content as (a) but plotted in logarithmic x-axis. (c) A scheme describes the electron transport through the interfaces of core and shell in nanowires. .... 99





